

Contrasting age-dependent leaf acclimation strategies drive vegetation greening across deciduous broadleaf forests in mid- to high latitudes

Received: 24 November 2024

Accepted: 30 July 2025

Published online: 08 September 2025



A list of authors and their affiliations appears at the end of the paper

Increasing leaf area and extending vegetation growing seasons are two primary drivers of global greening, which has emerged as one of the most significant responses to climate change. However, it remains unclear how these two leaf acclimation strategies would vary across forests at a large spatial scale. Here, using multiple satellite-based datasets and field measurements, we analysed the temporal changes (Δ) in maximal leaf area index (LAI_{max}) and length of the growing season (LOS) from 2002 to 2021 across deciduous broadleaf forests (DBFs) in the middle to high latitudes. Contrary to the widely held assumption of coordination, our results revealed a negative correlation between $\Delta\text{LAI}_{\text{max}}$ and ΔLOS . Notably, the trade-offs between $\Delta\text{LAI}_{\text{max}}$ and ΔLOS were strongly explained by stand age. Younger DBFs, with lower baseline LAI_{max} , predominantly located in eastern Asia, displayed an increase in LAI_{max} with small changes in LOS. This acquisitive strategy facilitated younger DBFs to grow more photosynthetically efficient leaves with low leaf mass per area, enhancing their light use efficiency. Conversely, older DBFs with a higher baseline LAI_{max} , primarily located in North America and Europe, extended their LOS by increasing leaf mass per area. This conservative strategy facilitated older DBFs to produce thicker, but less photosynthetically efficient leaves, resulting in decreased light use efficiency. Our findings offer new insights into the contrasting changes in leaf area and growing season length and highlight their divergent impacts on ecosystem functioning.

In recent decades, vegetation greening, defined as the increase of annual or seasonal vegetation greenness observed by satellites, has become one of the most significant responses of plants to climate change^{1–3}. This global greening encompasses a range of leaf acclimation strategies among plants worldwide, which have not been fully understood. One commonly observed strategy is to produce more canopy leaves^{4,5}, while another involves adjusting the timing of the growing season, by advancing its start (SOS)^{6,7} and/or delaying its end

(EOS)^{8,9}. The first strategy leads to an increase in maximum leaf area index (LAI_{max})^{10,11}, while the second results in an increase in the length of the growing season ($\text{LOS} = \text{EOS} - \text{SOS}$) (refs. 8,12–14). A fundamental question has been whether and how these two leaf acclimation strategies vary across biomes under climate change.

Satellite observations have recorded increases in LAI_{max} and LOS across deciduous broadleaf forests (DBFs)^{4,7,15–19}. The widely held belief is that LAI_{max} and LOS have changed coordinatively. Nevertheless,

✉ e-mail: chenxzh73@mail.sysu.edu.cn

according to the leaf economics spectrum theory, leaf trait trade-offs often occur within and among plant communities^{20,21}. Plants located at the ‘fast’ end of economics spectrum tend to produce thinner and more efficient leaves with a shorter lifespan, yielding a faster return on investment in terms of carbon gain relative to the resources invested in leaf construction, while plants located at the ‘slow’ end of the economics spectrum tend to adopt a conservative strategy and favour less efficient leaves with a longer leaf lifespan^{20,22,23}. In this context, young forests are expected to adopt an acquisitive strategy to grow more leaves for maximizing carbon gain under climate change^{21,24}. By contrast, old forests may follow a conservative strategy, prioritizing LOS extension to maximize photosynthesis over time^{21,24}. Based on this viewpoint, we hypothesize that forests at different growth stages respond differently to climate change (that is, increasing LAI_{max} or extending LOS). Although this reasoning is conceptually appealing, it has not yet been fully examined in the real world at large spatial scales. Addressing these knowledge gaps can enhance our understanding of the complex leaf acclimation strategies in response to climate change and their implications for ecosystem functioning (that is, productivity).

We leveraged multiple satellite-based datasets (Supplementary Table 1) and field measurements to investigate the LAI_{max} versus LOS acclimation strategies and their potential controls by stand age (denoted as A_{age}) at large spatial scales. We focused exclusively on DBFs in the middle to high latitudes (Supplementary Fig. 1; see ‘Selecting DBFs without disturbances’ section in Methods), which exhibit a LOS of less than 12 months and moderate LAI (typically LAI < 6.0 m² m⁻²). Thus, the LAI metric in this biome exhibits less saturation and remains sensitive to vegetation density^{25,26}. We first examined the correlations between decadal changes in LAI_{max} (defined as the average LAI between the maturity and senescence period; Supplementary Fig. 2) and in LOS (defined as the average LOS between the green-up and dormancy period) (denoted, respectively, as $\Delta\text{LAI}_{\text{max}}$ and ΔLOS) using satellite-based Global Land Surface Satellite (GLASS) LAI product²⁷ and Moderate Resolution Imaging Spectroradiometer (MODIS) leaf phenology dataset²⁸ during 2002–2021 (see ‘Exploring relationships between $\Delta\text{LAI}_{\text{max}}$ and ΔLOS ’ section in Methods). Then, we used satellite-derived leaf moisture content (LMC) (2002–2016)²⁹ and leaf mass per area (LMA) estimated from MODIS reflectance data^{30–32} via the PROSAIL model^{33,34} to investigate potential changes in leaf traits alongside variations in LAI_{max} and LOS. Satellite observations were validated against field measurements of LMA and LMC from the widely referenced TRY Plant Trait database^{35,36}. Finally, we assessed the cascading impacts on light use efficiency (LUE), defined as the ratio of gross primary production (GPP) to absorbed photosynthetically active radiation (APAR) using data-driven GPP from Breathing Earth System Simulator (BESS, v2.0), PAR from GLASS (04B01.V60) and the fraction of absorbed PAR (fAPAR) from GLASS (09B01.V60)^{37–39}.

Results

Negative correlation between $\Delta\text{LAI}_{\text{max}}$ and ΔLOS

We found that DBFs displayed contrasting patterns in $\Delta\text{LAI}_{\text{max}}$ and ΔLOS during the period 2002–2021, with a small but significant negative linear correlation ($R = -0.16$; $P < 0.001$) (Fig. 1a–c). Overall, DBFs with LOS extensions ($\Delta\text{LOS} > 5.0$ days) were primarily located in North America (32%) and Europe (16%) (Fig. 1b), together accounting for 48% of the study areas. By contrast, 39% of the studied DBFs showed an increase in LAI_{max} ($\Delta\text{LAI}_{\text{max}} > 0.1$ m² m⁻²), mostly clustered in eastern Asia (22.22%) and scattered across Europe (3%) (Fig. 1a).

Interestingly, the negative relationship between $\Delta\text{LAI}_{\text{max}}$ and ΔLOS was strongly explained by stand age (A_{age}), with $\Delta\text{LAI}_{\text{max}}$ sharply decreasing (slope -1.73×10^{-3} m² m⁻² yr⁻¹) and ΔLOS increasing (slope 7.85×10^{-2} days yr⁻¹) as A_{age} increased (Fig. 1d,e). Younger DBFs with a lower baseline $\Delta\text{LAI}_{\text{max}}$ maintained a larger Area_{leaf}/Area_{sapwood} ratio, representing the ratio of total leaf area (Area_{leaf}) to the sapwood cross-sectional area (Area_{sapwood})^{40,41} (Supplementary Fig. 3b,c).

Consequently, younger DBFs in Asia with smaller A_{age} could afford a substantial increase in $\Delta\text{LAI}_{\text{max}}$ (Fig. 1a). By contrast, older DBFs with higher baseline $\Delta\text{LAI}_{\text{max}}$ showed a relatively lower Area_{leaf}/Area_{sapwood} ratio (Supplementary Fig. 3b,c). As a result, older DBFs in North America and Europe with larger A_{age} appeared to produce less additional leaf growth (Fig. 1a). Instead, they markedly advanced the SOS and/or delayed the EOS (Supplementary Fig. 4), resulting in a notable increase in LOS (Fig. 1b).

Changes in leaf physics and chemistry

$\Delta\text{LAI}_{\text{max}}$ and ΔLOS can be associated with different changes in the physical and chemical properties of leaves across DBFs with varying A_{age} . LMA is a leaf trait highly related to leaf chemical properties such as nitrogen, phosphorus and potassium content⁴². Therefore, we explored the temporal changes in LMA (ΔLMA) during the period 2002–2016 and used ΔLMA as a proxy to investigate leaf chemical variability across DBFs with different A_{age} . In addition, we assessed the temporal changes in LMC (ΔLMC) during the period 2002–2016 based on the time-series MODIS-derived LMC datasets²⁹ and used ΔLMC as a proxy to examine leaf physical variability (refer to ‘Exploring leaf physical, chemical and functional changes’ and ‘Modelling LMA using the PROSAIL model’ sections in Methods for details).

We found that both ΔLMA and ΔLMC were positively correlated with A_{age} ($P < 0.001$) (Fig. 2). Specifically, younger forests in eastern Asia (regionally averaged $A_{\text{age}} = 54.29 \pm 0.14$ years) showed decreases in LMA by 1.39 mg cm⁻² and in LMC by 1.18% during the study period (Supplementary Fig. 5). This suggested that, with ongoing climate change, younger DBFs tended to produce more, thinner leaves with lower LMC. Conversely, older DBFs exhibited larger positive ΔLMA and ΔLMC values (Fig. 2b,d). For instance, in North America and Europe, where the regionally averaged A_{age} was 77.23 years, LMA increased by 1.27 mg cm⁻² and 1.94 mg cm⁻², while LMC increased by 5.55% and 8.72%, respectively (Supplementary Fig. 5). These results indicated that older DBFs tended to develop thicker leaves with higher LMC, promoting leaf longevity under climate change. The satellite-based results were further validated using field observations of specific leaf area (SLA) and leaf dry matter content (LDMC) from the TRY dataset^{35,36} (Supplementary Fig. 6; see ‘Validations using in situ SLA and LDMC data’ section in Methods), where SLA is the reciprocal of LMA, and LDMC is complementary to LMC, respectively^{43,44}. These analyses also showed negative correlations between SLA, LDMC and A_{age} , aligning with the satellite-inferred findings (Fig. 2b,d).

Overall, the contrasting changes in leaf properties between younger and older DBFs were associated with the age-dependent negative correlations between $\Delta\text{LAI}_{\text{max}}$ and ΔLOS .

Implications for ecosystem functioning

The contrasting changes in leaf physical and chemical properties between younger and older DBFs can lead to cascading effects on ecosystem photosynthesis. To examine this, we quantified temporal changes in LUE (ΔLUE) over the 2002–2016 period and used structural equation modelling (SEM) to investigate the main paths through which leaf traits (LMA versus LMC) might impact LUE (Fig. 3a,b). To eliminate the impacts of climate variability, we applied the SEM analyses within each 2° × 2° moving window and calculated the regionally averaged path coefficient (R_{pc}) of ΔLMA versus ΔLMC impact on ΔLUE (Fig. 3c).

Results indicated that decreases in LMA, usually alongside the increase in canopy leaves, primarily enhanced LUE ($R_{\text{pc}} = -0.117$). For instance, younger forests in eastern Asia (Fig. 3a), where leaf acclimation favoured thinner leaves (Fig. 4a), exhibited a substantial increase in ecosystem LUE ($\Delta\text{LUE} = 2.38 \times 10^{-3} \pm 5.10 \times 10^{-5}$ gC J⁻¹) (Fig. 3b). By contrast, older forests, primarily located in North America and Europe (Fig. 3a), experienced significant declines in LUE ($\Delta\text{LUE} = -7.31 \times 10^{-4} \pm 4.12 \times 10^{-5}$ gC J⁻¹) (Fig. 3b). These declines were linked to the extension of LOS accompanied by widespread increases

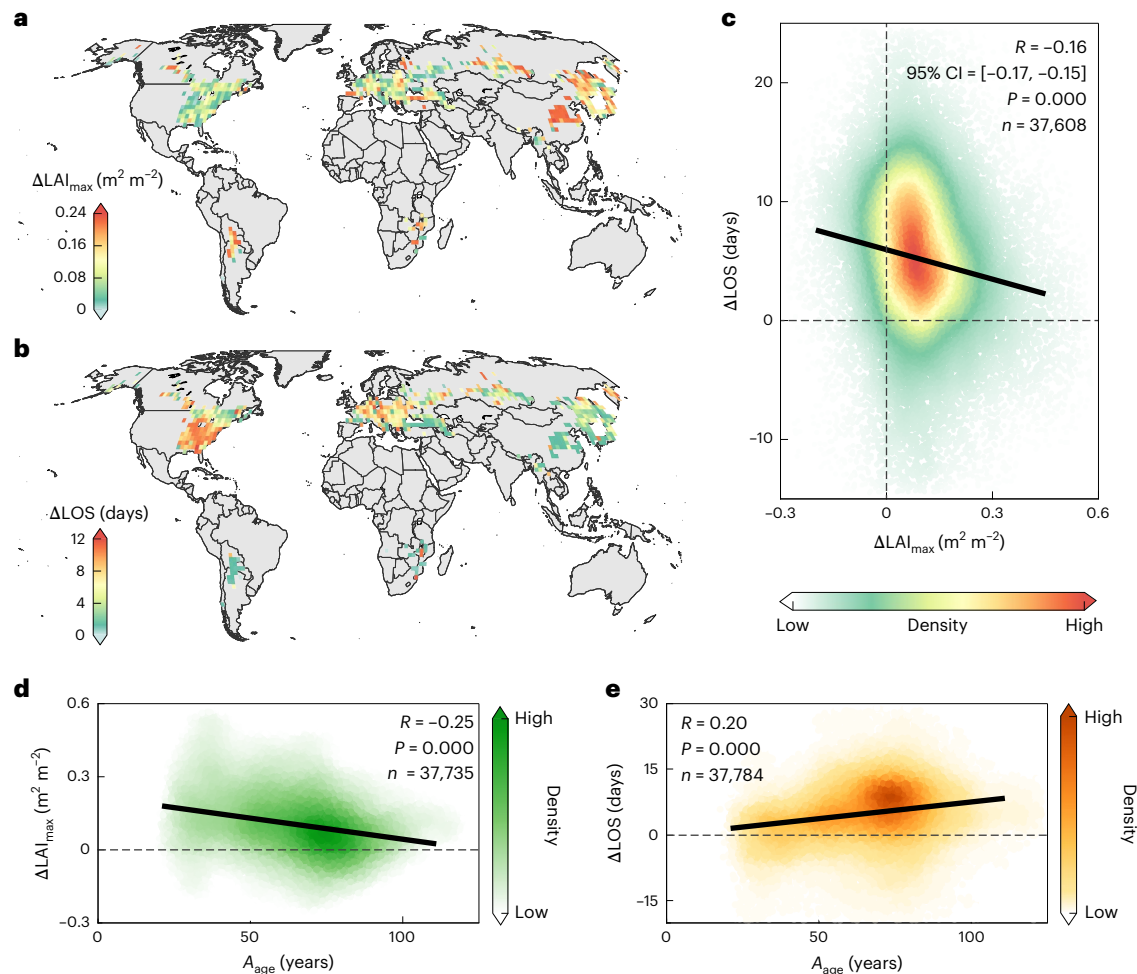


Fig. 1 | Contrasting changes in maximal leaf area index ($\Delta\text{LAI}_{\text{max}}$) and length of growing season (ΔLOS) from 2002 to 2021 across DBFs in the middle to high latitudes. **a, Map of $\Delta\text{LAI}_{\text{max}}$ during the 2002–2021 period. **b**, Map of ΔLOS during the 2002–2021 period. **c**, Negative correlation between $\Delta\text{LAI}_{\text{max}}$ and ΔLOS , with the black line representing the linear regression between two variables. The 95% confidence interval (CI) of the Pearson's correlation coefficient (R) in the square brackets was tested by using the Fisher's z**

transformation. **d**, Negative correlation between $\Delta\text{LAI}_{\text{max}}$ and stand age (A_{age}). **e**, Positive correlation between ΔLOS and stand age (A_{age}). The black lines in **d** and **e** represent the linear regressions between $\Delta\text{LAI}_{\text{max}}$ and A_{age} and between ΔLOS and A_{age} , respectively. A_{age} data were extracted from the widely used MPI-BGC global forest dataset⁷⁴. In **c–e**, the P values were evaluated using a two-sided Student's t -test.

in ΔLMA ($\Delta\text{LMA} = 1.26 \pm 0.02 \text{ mg cm}^{-2}$; $R_{\text{pc}} = -0.117$) and ΔLMC ($\Delta\text{LMC} = 7.12 \pm 0.10\%$; $R_{\text{pc}} = -0.142$) (Fig. 3c). This driving mechanism of leaf physical and chemical changes impact on LUE, as illustrated by the SEM analyses, remained robust across various A_{age} bins (Supplementary Fig. 7). Overall, younger forests tended to grow thinner leaves with higher photosynthetic efficiency to enhance LUE, while older forests tended to develop thicker leaves with a longer lifespan but lower photosynthetic efficiency, leading to reduced LUE (Fig. 4).

Potential uncertainties and caveats

A key issue to consider is the validity of a dynamic phenological extraction threshold method to extract LOS⁴⁵. This approach uses a dynamic threshold of the 2-band Enhanced Vegetation Index (EVI2) to determine the start (SOS) and end (EOS) of the growing season based on the seasonal cycle of EVI2 data⁴⁶. The EVI2 threshold (denoted as EVI2_0 in equation (1)) is defined as a linear function of two extreme EVI2 values: EVI2_{min} (the minimum of EVI2) and EVI2_{max} (the maximum of EVI2). While EVI2_{min} remains relatively stable, EVI2_{max} varies annually and can influence the value of EVI2_0 , leading to uncertainties in LOS estimation ($\Delta\text{LOS}_{\text{uncertainty}}$) (refer to 'Exploring relationships between $\Delta\text{LAI}_{\text{max}}$ and ΔLOS ' section in Methods for details). Specifically, EVI2_{max} increases in the case of greening and may cause a rise in EVI2_0 ,

leading to an overall shorter LOS ($\Delta\text{LOS}_{\text{uncertainty}} < 0$). This may artificially introduce a negative correlation between ΔLOS ($\Delta\text{LOS} < 0$) and $\Delta\text{LAI}_{\text{max}}$ ($\Delta\text{LAI}_{\text{max}} > 0$). Therefore, accounting for uncertainties associated with the dynamic LOS extraction threshold method is crucial for confirming the robustness of the satellite-observed contrasting changes in LAI_{max} and LOS. To address this, we first applied a dynamic phenological threshold to the EVI2 curve to reproduce the MODIS phenology product (Supplementary Fig. 8a,b). Second, we quantified $\Delta\text{LOS}_{\text{uncertainty}}$ associated with changes in EVI2_{max} ($\Delta\text{EVI2}_{\text{max}}$) (see 'Exploring relationships between $\Delta\text{LAI}_{\text{max}}$ and ΔLOS ' section in Methods). As expected, the dynamic phenological threshold method could result in negative correlations between $\Delta\text{EVI2}_{\text{max}}$ and $\Delta\text{LOS}_{\text{uncertainty}}$, but such impacts are overall minor (Supplementary Fig. 8c,d). By subtracting $\Delta\text{LOS}_{\text{uncertainty}}$ from the corresponding ΔLOS for each pixel, results still showed a significant ($P < 0.001$) negative relationship between $\Delta\text{LAI}_{\text{max}}$ and ΔLOS (Supplementary Fig. 8f). We further used fixed EVI2 thresholds (0.2, 0.25 and 0.30) to extract SOS and EOS, which were then used to compute LOS. The observed negative relationship between $\Delta\text{LAI}_{\text{max}}$ and ΔLOS still held true (Supplementary Fig. 9).

To minimize impacts from interannual data variability, we examined the negative correlations between $\Delta\text{LAI}_{\text{max}}$ and ΔLOS across different time frames, randomly selected for each pixel. These analyses

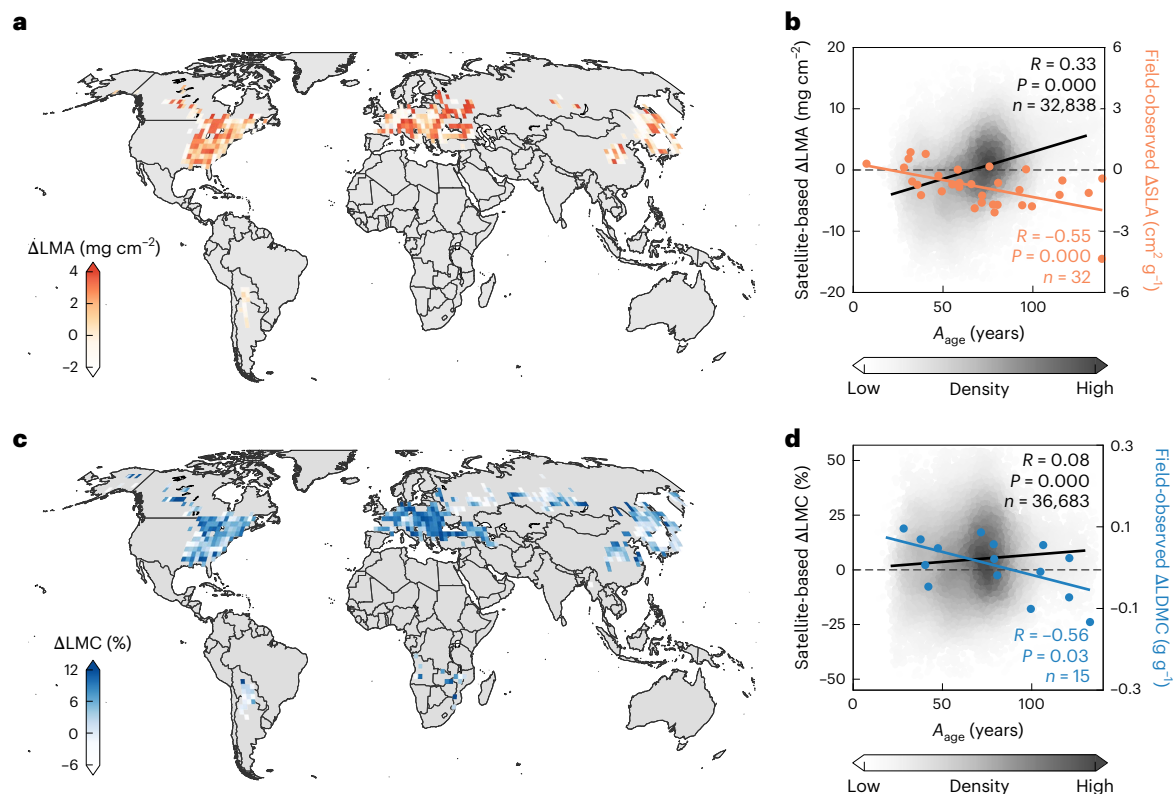


Fig. 2 | Temporal changes in leaf mass per area (Δ LMA) and leaf moisture content (Δ LMC) from 2002 to 2016 across DBFs in the middle to high latitudes.

a, Map of Δ LMA during the 2002–2016 period. **b**, Positive correlations between Δ LMA and stand age (A_{age}). The black dots indicate the satellite-based Δ LMA data. The black line represents the linear regressions between Δ LMA and A_{age} . The SLA is the reciprocal of LMA⁴³. The orange dots indicate the field-observed Δ SLA data. The orange line represents the linear regressions between Δ SLA and A_{age} . **c**, Map of Δ LMC between the same two periods. **d**, Positive correlations between Δ LMC and A_{age} . The black dots indicate satellite-based Δ LMC data.

The black line represents the linear regressions between Δ LMC and A_{age} . The LDMC is complementary to LMC⁴⁴. The blue dots indicate the field-observed Δ LDMC data. The blue line represents the linear regressions between Δ LDMC and A_{age} . The field-observed Δ SLA and Δ LDMC were both evaluated within each $2^\circ \times 2^\circ$ grid cell (refer to ‘Exploring leaf physical, chemical and functional changes’, ‘Modelling LMA using the PROSAIL model’ and ‘Validations using in situ SLA and LDMC data’ sections in Methods for details). In **b** and **d**, the P values were calculated using a two-sided Student’s t -test.

further confirmed the robustness of our findings regarding this negative relationship (Supplementary Fig. 10). In addition, we calculated the slope of the linear correlation between the time series of LAI_{max} ($\text{slope}_{\text{LAI}_{\text{max}}}$), LOS ($\text{slope}_{\text{LOS}}$) and time (also known as a linear trend or temporal trend). The results also showed negative correlations between $\text{slope}_{\text{LAI}_{\text{max}}}$ and $\text{slope}_{\text{LOS}}$ (Supplementary Fig. 11). These analyses showed that the contrasting changes in LAI_{max} and LOS reflected a biological reality rather than an artefact of a specific phenological extraction method or random temporal variability.

Uncertainties may also arise from tree cover changes, which can influence both the sign and magnitude of $\Delta\text{LAI}_{\text{max}}$. To address this, we classified DBFs into four groups based on their tree cover fraction: 50–60%, 60–70%, 70–80% and >80%. For each group, we analysed the relationship between $\Delta\text{LAI}_{\text{max}}$ and ΔLOS within different tree cover change bins (0–1%, 1–2%, 2–3%, 3–4% and 4–5%). Results consistently showed negative correlations between $\Delta\text{LAI}_{\text{max}}$ and ΔLOS across all tree cover change bins, confirming the robustness of our findings (Supplementary Fig. 12). Extreme climate events may also introduce uncertainties. For instance, our analysis showed that droughts could reduce $\Delta\text{LAI}_{\text{max}}$, which in turn weakened the negative correlations between $\Delta\text{LAI}_{\text{max}}$ and ΔLOS (Supplementary Fig. 13). Under drought conditions, the acclimation of leaf chemical and physical properties played a less important role in regulating LUE (Supplementary Fig. 14).

Furthermore, correlations between $\Delta\text{LAI}_{\text{max}}$ and ΔLOS may vary across tree species. To examine this, we analysed field-observed phenological data of the USA National Phenology Network⁴⁷ (Supplementary

Fig. 15), the Pan European Phenological database⁴⁸ (Supplementary Fig. 16) and the northern Eurasia Phenological database⁴⁹ (Supplementary Fig. 17) against the MODIS EVI product at a higher resolution of 250 m (ref. 50) (see ‘Validations using in situ and high-resolution satellite data’ section in Methods). Results showed that field-observed ΔLOS in most species remained positively correlated with A_{age} . The $\Delta\text{EVI}_{\text{max}}$ also exhibited a negative correlation with ΔLOS . However, the relationship between $\Delta\text{EVI}_{\text{max}}$ and A_{age} may vary considerably across species.

Overall, although the negative $\Delta\text{LAI}_{\text{max}}-\Delta\text{LOS}$ relationship observed in this study is generally robust, uncertainties remain due to limitations in field-based LAI and leaf trait data, the coarse resolution of satellite observations and the complexity of forest communities across local to global scales.

Discussion

A key finding of this study is the contrasting changes in leaf area and growing season length in DBFs across various stand ages. While climate change has driven widespread global greening⁴, it remains unexplored at large scales whether increases in maximal leaf area^{4,5} and extension in growing seasons coordinate or trade off with each other^{51–54}. Here, we observed that younger forests with a lower baseline LAI favour the growth of additional thinner leaves^{55–57}. By contrast, older forests with a higher baseline LAI prioritize extensions of growing season length over additional leaf growth^{58,59}. This finding enhances our understanding of global vegetation greening and highlights the necessity of considering different leaf acclimation strategies (that is, growing new leaves

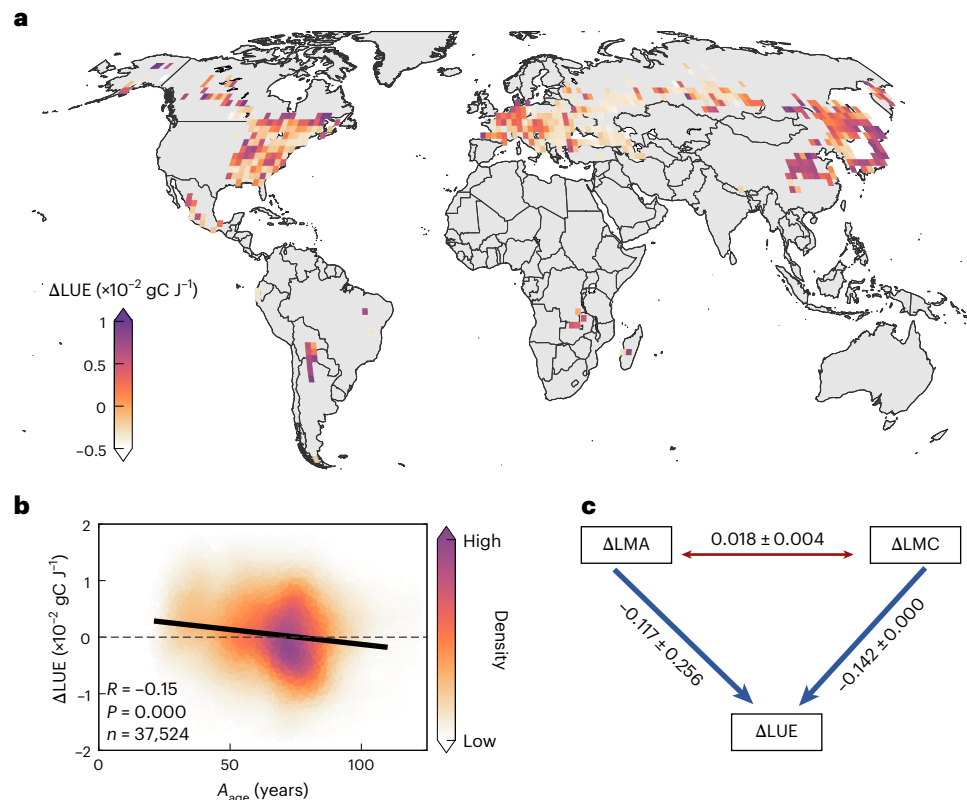


Fig. 3 | Cascading influences on changes in ecosystem light use efficiency (ΔLUE) from 2002 to 2016 across DBFs in the middle to high latitudes. **a, Map of ΔLUE during the 2002–2016 period. **b**, Negative correlation between A_{age} and ΔLUE . The black line represents the linear regression between ΔLUE and A_{age} . The P values were calculated using a two-sided Student's t -test. **c**, SEM of the paths of**

changes in leaf physical and chemical properties (ΔLMA and ΔLMC) impacting ΔLUE . The path coefficients were the average values of corresponding path coefficients in the SEM model applied in each $2^\circ \times 2^\circ$ moving window across the selected DBFs.

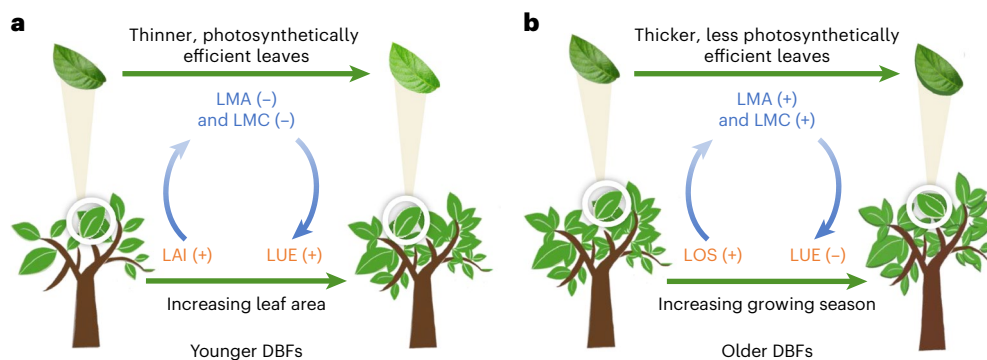


Fig. 4 | Schematic representation of age-dependent leaf acclimation strategies driving vegetation greening across DBFs in the middle to high latitudes. **a, Younger DBFs tend to develop thinner and more photosynthetically efficient leaves. **b**, Older DBFs tend to extend the growing season with thicker but less photosynthetically efficient leaves.**

versus extending growing season longevity) when modelling the foliar phenological shifts under climate change.

The divergent changes in leaf properties identified in this study align with the classic leaf economics spectrum theory, which emphasizes such trade-offs^{20,21}. Younger forests located at the ‘fast’ end of the economics spectrum tended towards an acquisitive strategy^{21,24}. With climate change, these forests produced more thinner leaves with a lower percentage water content, constraining the extension of growing season and shifting canopy towards higher photosynthetic capacity leaves^{3,60–62}. We showed that forests adopting a ‘fast’ economics strategy were characterized by an increase in LAI_{max} , accounting for 39% of DBFs in the middle to high latitudes. Conversely, as community

succession progressed, forest ecosystems tended to contain more older trees, which may shift towards a more conservative strategy^{21,24}. These forests (48% of DBFs) predominantly followed a ‘slow’ economics strategy, mostly extending their LOS by producing thicker leaves with a higher percentage water content that could remain on the canopy for longer⁴³. Consequently, this acclimation strategy tended to reduce ecosystem LUE^{63–66}.

In summary, we found a negative correlation between changes in maximal LAI and growing season length. These contrasting changes were strongly influenced by stand age, reflecting contrasting leaf acclimation between younger and older forests. These strategies led to distinct changes in LMA and LMC, with cascading impacts on carbon

fluxes. Our findings emphasized the importance of accounting for diverse leaf acclimation strategies to fully understand the relationships among changes in leaf area, growing seasons, leaf physics and leaf chemistry, and their effects on ecosystem functioning under climate change.

Methods

Selecting DBFs without disturbances

Our study focused on DBFs in the middle to high latitudes with a defined leaf lifespan (<12 months) and moderate LAI ($\text{LAI} < 6.0 \text{ m}^2 \text{ m}^{-2}$), which exhibited minimal saturation issues in satellite signals^{25,26}. We selected 0.05° -resolution grid cells classified as DBFs with tree cover >50% in the MODIS MCD12C1 V061 land cover imagery from 2002 to 2021⁶⁷. Notably, we excluded DBFs in tropical forests that may have different climatic drivers from those in mid-to-high latitudes. To minimize the impacts of natural disturbances and land cover changes, we overlaid 30 m high-resolution global tree cover change maps from Global Forest Watch⁶⁸ onto the 0.05° -resolution MODIS land cover images, excluding grid cells with tree cover changes greater than 5% over the study period⁶⁹. We retained only DBF grid cells with consistent land cover type (within 0 ± 0.05 fraction) from 2002 to 2021. To ensure robustness, we controlled tree cover changes within small bins to test our key findings of this study (Supplementary Fig. 12). In addition, we excluded pixels affected by wildfires by removing 0.05° forest grid cells with burned areas during the study period, using the MODIS Fire_cci AVHRR-LTDR Burned Area Pixel product (version 1.1)⁷⁰, which provides a 0.05° spatial and monthly temporal resolution.

Moreover, extreme climatic events such as droughts can introduce variability in LAI and phenology. To account for this, we classified the studied DBFs into several drought groups. Pixels that experienced severe drought events were used to assess the impacts of drought on these responses (Supplementary Fig. 13). Notably, a month was classified as experiencing severe drought if the anomaly of Palmer Drought Severity Index^{71,72} fell more than 1.5 standard deviation below the 2002–2021 monthly mean⁷³. A year was considered as a drought year for a given pixel if it experienced four consecutive months of drought between the start (SOS) and end (EOS) dates of the growing season period (see definition in ‘Exploring relationships between $\Delta\text{LAI}_{\text{max}}$ and ΔLOS ’ section). Notably, for each given pixel, we identified the SOS and EOS for each year and used the multiple-year averaged SOS and EOS as the time nodes to count the drought events during the study period.

Exploring relationships between $\Delta\text{LAI}_{\text{max}}$ and ΔLOS

We utilized the GLASS LAI (O1B01.V60) product (2002–2021)²⁷, with a spatial resolution of 0.05° and an 8-day temporal resolution, to calculate $\Delta\text{LAI}_{\text{max}}$. During this period, the GLASS LAI data were derived from MODIS surface reflectance data using the bidirectional LSTM deep learning model²⁷. We first downloaded the Maturity_1 and Senescence_1 layers from the MODIS global vegetation characterization product (MCD12Q2, 500 m resolution)²⁸ via Google Earth Engine at a 0.05° resolution. These layers represented the dates when EVI2 first (leaf maturity) and last (leaf senescence) crossed the 90% of the segment amplitude threshold²⁸, corresponding to the leaf maturity and senescence stages, respectively. We then calculated the mean LAI during this period as LAI_{max} for each pixel (Supplementary Fig. 2).

We used the MCD12Q2 phenology products to calculate ΔLOS . The MCD12Q2 phenology products used a dynamic phenological extraction threshold (EVI2_0) based on a simple linear function (equation (1)) of the minimal (EVI2_{min}) and maximal (EVI2_{max}) values of EVI2 to determine the start (SOS) and end (EOS) dates of the growing season²⁸:

$$\text{EVI2}_0 = \text{EVI2}_{\text{min}} + 15\% \times (\text{EVI2}_{\text{max}} - \text{EVI2}_{\text{min}}), \quad (1)$$

where EVI2_0 represents the dynamic threshold of EVI2 used to identify SOS and EOS.

SOS is defined as the day when the EVI2 seasonal curve crosses EVI2_0 within the green-up segment, while EOS is defined as the day when the EVI2 curve crosses EVI2_0 within the green-down segment.

The layers of Greenup_1 and Dormancy_1 in the MCD12Q2 product (version 6.1) were produced on the basis of equation (1) to represent SOS and EOS, respectively. Here, we computed the length of the growing season (LOS) using equation (2).

$$\text{LOS} = \text{EOS} - \text{SOS}. \quad (2)$$

Notably, the MCD12Q2 time series after 2012 were corrected using a different method than those used for the time series before 2012⁴⁶, leading to potential discontinuity for LOS time series. Thus, in this study, temporal changes in LOS, denoted as ΔLOS , were calculated as the mean of ΔLOS between the periods 2002–2004 and 2010–2012 and ΔLOS between the periods 2013–2015 and 2019–2021 (Fig. 1b). The same was done for calculating corresponding $\Delta\text{LAI}_{\text{max}}$ (Fig. 1a).

To assess uncertainties caused by interannual data variability, we randomly selected different time frames to calculate $\Delta\text{LAI}_{\text{max}}$ and ΔLOS . Specifically, for each pixel, we used the MATLAB’s random number generators to randomly generate pairs of years that were at least 5 years apart from each other within the study period. Then, we calculated the $\Delta\text{LAI}_{\text{max}}$ and ΔLOS between each randomly selected pair of years. This random sampling approach was applied to all pixels independently to ensure that the time frame for each pixel was set randomly. Similarly, to mitigate potential impacts from this discontinuity before and after 2012, the random time frame testing was performed for the periods 2002–2012 and 2013–2021, respectively (Supplementary Fig. 10). In addition, we tested the contrasting change in LAI_{max} and LOS with time using temporal trends for the periods 2002–2012 and 2013–2021, respectively (Supplementary Fig. 11). The trends of temporal changes in LAI_{max} and LOS were defined as the slopes of the linear correlation between time-series of LAI_{max} ($\text{slope}_{\text{LAI}_{\text{max}}}$), LOS ($\text{slope}_{\text{LOS}}$) and time.

To examine the relationship between $\Delta\text{LAI}_{\text{max}}$ and ΔLOS in DBFs with varying stand age (A_{age}), we used the widely adopted Max Planck Institute for Biogeochemistry (MPI-BGC) stand age (A_{age}) dataset at 1 km spatial resolution⁷⁴. The gridded A_{age} data were derived from a machine learning model trained on over 40,000 forest plots, integrating forest inventory data, biomass and climate variables⁷⁴. This dataset also accounts for variations in tree cover thresholds through aboveground biomass maps⁷⁴. We then analysed the changes in $\text{Area}_{\text{leaf}}/\text{Area}_{\text{sapwood}}$, LAI_{max} , LOS, leaf properties (LMA and LMC) and LUE with rising A_{age} . The sapwood area ($\text{Area}_{\text{sapwood}}$) data were obtained from Liu et al.⁴⁰ and He et al.⁴¹, while datasets for other leaf traits, such as LMA, LMC and LUE, are introduced in the following sections.

Notably, EVI2_0 in equation (1) depends on EVI2_{min} and EVI2_{max} . While EVI2_{min} remained relatively stable, EVI2_{max} varied annually, largely influencing the value of EVI2_0 and in turn introducing uncertainties in calculating ΔLOS (refer to the first paragraph in ‘Potential uncertainties and caveats’ section in the Results). In other words, ΔLOS computed using this method may be inherently related to $\Delta\text{LAI}_{\text{max}}$ (ref. 42). To account for this dependency, we replaced the EVI2_{max} of the starting year with that of the final year within the selected time frame to obtain new LOS data for each pixel. The differences between this new and the original LOS data were quantified as LOS uncertainties ($\Delta\text{LOS}_{\text{uncertainty}}$) caused by the dynamic phenological extraction threshold method (that is, changes in EVI2_{max}) (Supplementary Fig. 8). Furthermore, we also used three fixed EVI2 thresholds (0.2, 0.25 and 0.30) to extract SOS and EOS, and then LOS to test the robustness of the negative relationship between $\Delta\text{LAI}_{\text{max}}$ and ΔLOS (Supplementary Fig. 9).

Validations using in situ and high-resolution satellite data

We further validated the robustness of the negative correlations between $\Delta\text{LAI}_{\text{max}}$ and ΔLOS using higher-resolution satellite-based

MOD13Q1 v061 EVI⁵⁰ (<https://lpdaac.usgs.gov/products/mod13q1v061/>) and field-observed LOS data from global phenology networks^{47–49} (<http://www.pep725.eu/>; <https://doi.org/10.1038/s41597-020-0376-z> and <https://www.usanpn.org/results/data>). The MOD13Q1 EVI dataset (2002–2021) was derived from Terra sensors with a spatial resolution of 250 m and a temporal resolution of 16 days⁵⁰.

Field-based LOS data were calculated using the EOS and SOS information provided by the Pan European Phenology Network (PEP725)⁴⁸, the Russian ‘Chronicles of Nature’ Network⁴⁹ and the USA National Phenology Network⁴⁷. PEP725 offers over 13 million records for 201 species from 26,000 sites in Europe, with data dating back to 1868⁴⁸. The Russian ‘Chronicles of Nature’ Network provides data from 471 sites across Russia, Ukraine, Uzbekistan, Belarus and Kyrgyzstan⁴⁹, while the USA National Phenology Network includes 3,000 records across the USA⁴⁷. For the European and Russian observation sites, the SOS was defined using records coded as ‘BBCH11’, while the EOS was defined using codes of ‘BBCH94’. At the USA sites, SOS and EOS were defined on the basis of records of ‘Breaking leaf buds’ and ‘≥50% of leaves coloyred (deciduous)’, respectively. The LOS was calculated using equation (2).

Notably, we focused exclusively on DBF observation sites. To ensure the robustness of long-term phenological records, we included sites with more than 5 years of observations for the random time frame analysis in European and Russian observation sites. By contrast, for the USA, where SOS and EOS are generally shorter, we included sites with at least 2 years of observations. We calculated Δ LOS based on phenological time series records for each genus or species at each observation site. Specifically, Δ LOS was derived by subtracting the LOS in the initial year from that in the final year for each species at each site. For each site, we calculated Δ EVI_{max} using data corresponding to the years and time frames used to determine LOS. The results are shown in Supplementary Figs. 15–17.

Exploring leaf physical, chemical and functional changes

We used satellite-based LMC²⁹ products and model-derived LMA^{31,32} to examine the temporal changes in leaf physical and chemical properties. The daily LMC product (2002–2016) has a spatial resolution of 0.25° and provides global estimates of LMC with median, maximum and minimum values to capture uncertainty. This study used the median LMC values for analysis. LMA data were derived from canopy-level reflectance measurements from the MODIS MCD43A4 V6.1 (2002–2016) using the PROSPECT-5 and 4SAIL models^{31,32,75} (refer to the following section for the methods used in PROSPECT modelling of LMA based on satellite-derived canopy-level reflectance). We calculated interannual variability in growing-season (from the Greenup_1 to Dormancy_1 day) LMA (Δ LMA) and LMC (Δ LMC) between the periods 2002–2004 and 2014–2016 to investigate changes in leaf physical and chemical properties over time.

We calculated temporal changes in growing-season LUE, denoted as Δ LUE (the 2014–2016 period minus the 2002–2004 period), to assess their influences on ecosystem functioning. LUE was calculated by dividing GPP³⁷ by the product of photosynthetically active radiation (PAR)³⁸ and the fraction of absorbed PAR (fAPAR)³⁹. GPP data were derived from the BESS v2.0 model, a satellite-based coupled-process model for estimating global land–atmosphere fluxes³⁷. This GPP dataset, with a spatial resolution of 0.05°, spans from 1982 to 2019 and provides daily cumulative data validated against FLUXNET observations, demonstrating reliable performance across different spatial and temporal scales. The daily PAR and fAPAR data were sourced from the GLASSO4B01.V60 and GLASSO9B01.V60 products, respectively, both at a 0.05° spatial resolution. All the analysis data were resampled to a 0.05° resolution using bilinear interpolation.

$$\text{LUE} = \frac{\text{GPP}}{\text{fAPAR} \times \text{PAR}} \quad (3)$$

Modelling LMA using the PROSAIL model

The PROSPECT-5 model simulates leaf optical properties, specifically reflectance and transmittance across the 400–2,500 nm range⁷⁵, which includes visible, near-infrared and shortwave infrared wavelengths that are critical for studying plant physiological properties, based on parameters such as leaf structure (N , dimensionless), chlorophyll content (Cab), equivalent water thickness (Cw) and LMA³³. The 4SAIL model, meanwhile, simulates canopy reflectance, incorporating factors such as LAI, leaf angle distribution and soil background^{76,77}. The combined PROSAIL model, integrating both PROSPECT-5 and 4SAIL, enables detailed spectral simulations from leaf to canopy levels based on these leaf traits, making it a widely used tool for studying temporal changes in leaf traits and relative reflectance^{75,78}. In this study, we applied the PROSAIL model to derive LMA across DBFs in the middle to high latitudes during the 2002–2016 period⁷⁹.

First, we input the leaf trait parameters (Supplementary Table 2) into the PROSAIL model to simulate leaf-level reflectance across DBFs in the middle to high latitudes from 2002 to 2016. The maximum and minimum values for parameters such as N , LAI, Cab, LMA and Cw were primarily derived from remote sensing data and prior knowledge from the literature^{77,80–83}. Fixed values were assigned to parameters such as leaf brown pigment and the hot spot size parameter^{84,85}. For each set of input parameter values, the PROSAIL model simulated leaf reflectance across the 400–2,500 nm spectrum. Reflectance was then extracted for seven specific spectral bands (visible: 459–479 nm, 545–565 nm and 620–670 nm; near-infrared: 841–876 nm; shortwave infrared: 1,230–1,250 nm, 1,628–1,652 nm and 2,105–2,155 nm), matching the MODIS MCD43A4 reflectance imagery bands. These data were used to establish a look-up table, linking simulated leaf reflectance of the seven spectral bands to corresponding leaf traits such as LAI, Cab, LMA and Cw. Ultimately, 26,124,444 sets of reflectance and leaf traits were generated.

Next, we extracted satellite-observed reflectance for above-mentioned seven spectral bands from the MODIS Nadir BRDF-Adjusted Reflectance product (MCD43A4 V6.1) for each DBF grid cell during the 2002–2016 period. The MCD43A4 V6.1 product provides daily MODIS band 1–7 surface reflectance at 500 m resolution³⁰. To ensure data quality, we applied the quality assurance flag to exclude cloud-affected pixels. The optimal reflectance was determined when the mean squared error between the simulated and observed spectra was minimized, calculated using equation (4)⁸². The LMA corresponding to the optimal reflectance was determined as the model-simulated LMA for each DBF grid cell.

$$\text{MSE} = \frac{\sum_{\lambda=1}^n (R_{\text{measured},i} - R_{\text{LUT},i})^2}{n} \quad (4)$$

where MSE is the mean squared error, $R_{\text{measured},i}$ is a measured reflectance at wavelength i , $R_{\text{LUT},i}$ is a modelled reflectance at wavelength i , and n is the number of wavelengths.

Validations using in situ SLA and LDMC data

We further validated the temporal changes in model-simulated LMA and satellite-inferred LMC using field-observed SLA (7,855 records) and LDMC (4,363 records) data from the TRY database (<https://www.try-db.org/>) (Supplementary Fig. 6). SLA is the reciprocal of LMA, and LDMC is complementary to LMC^{43,44}. The TRY database is a global repository containing over 2.88 million entries across approximately 69,000 plant species^{35,36}. Due to the lack of long-term time series records for SLA and LDMC at individual sites, we averaged the site-level SLA and LDMC within each 2° × 2° spatial grid cell, and then calculated Δ SLA and Δ LDMC by subtracting the SLA and LDMC values of earlier years from those of later years. Results based on field observations showed contrasting patterns of SLA and LDMC against A_{age} , consistent with those of model-simulated LMA and satellite-inferred LMC (Fig. 2b,d, black dots and line).

Exploring impacts of Δ LMA and Δ LMC on Δ LUE

This study used SEM to investigate the paths through which Δ LMA and Δ LMC, along with climatic variability, influenced Δ LUE. The SEMs were constructed using the lavaan package in R (ref. 86). Path coefficients (R_p) between variables were used to evaluate model fit. Notably, spatial climate variability may also bring uncertain impacts on the Δ LMA– Δ LUE and Δ LMC– Δ LUE relationships in the SEM model. Thus, to eliminate the impacts from spatial climate variability, we applied the SEM modelling analysis within each $2^\circ \times 2^\circ$ moving window. The path coefficients in the SEM models in Fig. 3 and Supplementary Figs. 7 and 14 are the average values of corresponding path coefficients in the SEM model applied in each $2^\circ \times 2^\circ$ moving window across the selected DBFs. In addition, drought years were excluded from the SEM analysis in Fig. 3c, while analysis including the impacts of droughts are shown in Supplementary Fig. 14 for comparison.

Reporting summary

Further information on research design is available in the Nature Portfolio Reporting Summary linked to this article.

Data availability

All the relevant data come from publicly available sources. The GLASS LAI (01B01.V60) product is available at <http://www.glass.umd.edu/LAI/MODIS/0.05D/>; the satellite leaf unfolding and dormancy dates product is available at <https://lpdaac.usgs.gov/products/mcd12q2v061/>; the MPI-BGC stand age data are available at <https://doi.org/10.17871/ForestAgeBGI.2021>; the MODIS Nadir BRDF-Adjusted Reflectance (NBAR) products (MCD43A4) are available via Google Earth Engine at https://developers.google.com/earth-engine/datasets/catalog/MODIS_061_MCD43A4; the LMC data are available via Zenodo at <https://doi.org/10.5281/zenodo.6545571>; the BESS v2.0 GPP data are available at <https://www.environment.snu.ac.kr/bessv2>; the GLASS PAR (04B01.V60) product is available at <http://www.glass.umd.edu/PAR/>; the GLASS fAPAR (09B01.V60) product is available at <http://www.glass.umd.edu/FAPAR/MODIS/0.05D/>; the Global Land cover data are available at <https://lpdaac.usgs.gov/products/mcd12c1v061/>; the MOD13Q1 V061 EVI data are available at <https://lpdaac.usgs.gov/products/mod13q1v061/>; the in situ leaf unfolding date products of Europe, Russia and the USA, respectively, are available at <http://www.pep725.eu>, <https://doi.org/10.1038/s41597-020-0376-z> and <https://www.usanpn.org/data/observational>; the TRY database is available at <https://www.try-db.org/>; the MODIS FireCCI11 (version 1.1) data are available at <https://catalogue.ceda.ac.uk/uuid/b1bd715112ca43ab-948226d11d72b85e/>; the GFW Global Forest Change v1.9 data are available at <https://glad.earthengine.app/view/global-forest-change>; the Palmer Drought Severity Index data are available at <https://climate.northwestknowledge.net/TERRACLIMATE>.

Code availability

The code used for this study is available via Zenodo at <https://doi.org/10.5281/zenodo.15765680> (ref. 87).

References

- Guo, K. et al. Leaf morphogenesis: the multifaceted roles of mechanics. *Mol. Plant* **15**, 1098–1119 (2022).
- Liu, J. et al. Evidence for widespread thermal acclimation of canopy photosynthesis. *Nat. Plants* **10**, 1919–1927 (2024).
- Piao, S. et al. Leaf onset in the northern hemisphere triggered by daytime temperature. *Nat. Commun.* **6**, 6911 (2015).
- Zhu, Z. et al. Greening of the Earth and its drivers. *Nat. Clim. Change* **6**, 791–795 (2016).
- Jian, D. et al. Limited driving of elevated CO₂ on vegetation greening over global drylands. *Environ. Res. Lett.* **18**, 104024 (2023).
- Buitenwerf, R., Rose, L. & Higgins, S. I. Three decades of multi-dimensional change in global leaf phenology. *Nat. Clim. Change* **5**, 364–368 (2015).
- Chen, C. et al. China and India lead in greening of the world through land-use management. *Nat. Sustain.* **2**, 122–129 (2019).
- Wu, C. et al. Contrasting responses of autumn-leaf senescence to daytime and night-time warming. *Nat. Clim. Change* **8**, 1092–1096 (2018).
- Chen, C. et al. Biophysical impacts of Earth greening largely controlled by aerodynamic resistance. *Sci. Adv.* **6**, eabb1981 (2020).
- Xia, J. et al. Joint control of terrestrial gross primary productivity by plant phenology and physiology. *Proc. Natl Acad. Sci. USA* **112**, 2788–2793 (2015).
- Huang, K. et al. Enhanced peak growth of global vegetation and its key mechanisms. *Nat. Ecol. Evol.* **2**, 1897–1905 (2018).
- Zhu, W. et al. Extension of the growing season due to delayed autumn over mid and high latitudes in North America during 1982–2006. *Glob. Ecol. Biogeogr.* **21**, 260–271 (2012).
- Fu, Y. H. et al. Declining global warming effects on the phenology of spring leaf unfolding. *Nature* **526**, 104–107 (2015).
- Zani, D. et al. Increased growing-season productivity drives earlier autumn leaf senescence in temperate trees. *Science* **370**, 1066–1071 (2020).
- Menzel, A. & Fabian, P. Growing season extended in Europe. *Nature* **397**, 659 (1999).
- Gunderson, C. A. et al. Forest phenology and a warmer climate—growing season extension in relation to climatic provenance. *Glob. Change Biol.* **18**, 2008–2025 (2012).
- Liu, Q. et al. Extension of the growing season increases vegetation exposure to frost. *Nat. Commun.* **9**, 426 (2018).
- Wang, X. et al. No trends in spring and autumn phenology during the global warming hiatus. *Nat. Commun.* **10**, 2389 (2019).
- Piao, S. et al. Characteristics, drivers and feedbacks of global greening. *Nat. Rev. Earth Environ.* **1**, 14–27 (2020).
- Reich, P. B., Walters, M. B. & Ellsworth, D. S. Leaf life-span in relation to leaf, plant, and stand characteristics among diverse ecosystems. *Ecol. Monogr.* **62**, 365–392 (1992).
- Wright, I. J. et al. The worldwide leaf economics spectrum. *Nature* **428**, 821–827 (2004).
- Reich, P. B., Walters, M. B. & Ellsworth, D. S. From tropics to tundra: global convergence in plant functioning. *Proc. Natl Acad. Sci. USA* **94**, 13730–13734 (1997).
- Reich, P. B. & Flores-Moreno, H. Peeking beneath the hood of the leaf economics spectrum. *N. Phytol.* **214**, 1395–1397 (2017).
- Chazdon, R. L. Beyond deforestation: restoring forests and ecosystem services on degraded lands. *Science* **320**, 1458–1460 (2008).
- Yan, K. et al. Performance stability of the MODIS and VIIRS LAI algorithms inferred from analysis of long time series of products. *Remote Sens. Environ.* **260**, 112438 (2021).
- Gao, S. et al. Evaluating the saturation effect of vegetation indices in forests using 3D radiative transfer simulations and satellite observations. *Remote Sens. Environ.* **295**, 113665 (2023).
- Ma, H. & Liang, S. Development of the GLASS 250-m leaf area index product (version 6) from MODIS data using the bidirectional LSTM deep learning model. *Remote Sens. Environ.* **273**, 112985 (2022).
- Friedl, M., Gray, J., & Sulla-Menashe, D. MODIS/Terra+ Aqua Land Cover Dynamics Yearly L3 Global 500 m SIN Grid V061. NASA EOSDIS Land Processes DAAC <https://doi.org/10.5067/MODIS/MCD12Q2.061> (2022).
- Forkel, M. et al. Estimating leaf moisture content at global scale from passive microwave satellite observations of vegetation optical depth. *Hydrol. Earth Syst. Sci.* **27**, 39–68 (2023).

30. Schaaf, C. & Wang, Z. MODIS/Terra+Aqua BRDF/Albedo Nadir BRDF Adjusted Ref Daily L3 Global - 500m V061. NASA EOSDIS Land Processes DAAC <https://doi.org/10.5067/MODIS/MCD43A4.061> (2021).
31. Féret, J.-B. et al. Estimating leaf mass per area and equivalent water thickness based on leaf optical properties: potential and limitations of physical modeling and machine learning. *Remote Sens. Environ.* **231**, 110959 (2019).
32. Sun, J. et al. Analyzing the performance of PROSPECT model inversion based on different spectral information for leaf biochemical properties retrieval. *ISPRS J. Photogramm. Remote Sens.* **135**, 74–83 (2018).
33. Jacquemoud, S. & Baret, F. PROSPECT: a model of leaf optical properties spectra. *Remote Sens. Environ.* **34**, 75–91 (1990).
34. Jacquemoud, S. et al. Estimating leaf biochemistry using the PROSPECT leaf optical properties model. *Remote Sens. Environ.* **56**, 194–202 (1996).
35. Kattge, J. et al. TRY—a global database of plant traits. *Glob. Change Biol.* **17**, 2905–2935 (2011).
36. Kattge, J. et al. TRY plant trait database—enhanced coverage and open access. *Glob. Change Biol.* **26**, 119–188 (2020).
37. Li, B. et al. BESSv2.0: a satellite-based and coupled-process model for quantifying long-term global land–atmosphere fluxes. *Remote Sens. Environ.* **295**, 113696 (2023).
38. Zhang, X. et al. Generating Global Land Surface Satellite incident shortwave radiation and photosynthetically active radiation products from multiple satellite data. *Remote Sens. Environ.* **152**, 318–332 (2014).
39. Ma, H. et al. Global land surface 250-m 8-day fraction of absorbed photosynthetically active radiation (FAPAR) product from 2000 to 2020. *Earth Syst. Sci. Data* **14**, 5333–5347 (2022).
40. Liu, F. et al. Variations in orthotropic elastic constants of green Chinese Larch from pith to sapwood. *Forests* **10**, 456 (2019).
41. He, P. et al. Growing-season precipitation is a key driver of plant leaf area to sapwood area ratio at the global scale. *Plant, Cell Environ.* **48**, 746–755 (2025).
42. Kikuzawa, K., & Lechowicz, M. J. *Ecology of Leaf Longevity* (Springer, 2011).
43. Poorter, H. et al. Causes and consequences of variation in leaf mass per area (LMA): a meta-analysis. *N. Phytol.* **182**, 565–588 (2009).
44. Wang, Z. et al. Leaf water content contributes to global leaf trait relationships. *Nat. Commun.* **13**, 5525 (2022).
45. Zhang, Y. et al. Autumn canopy senescence has slowed down with global warming since the 1980s in the Northern Hemisphere. *Commun. Earth Environ.* **4**, 173 (2023).
46. Gray, J., Sulla-Menashe, D. & Friedl, M. A. User guide to Collection 6 MODIS land cover dynamics (MCD12Q2) product. NASA EOSDIS Land Process. DAAC **6**, 1–8 (2019).
47. Schwartz, M. D., Betancourt, J. L. & Weltzin, J. F. From Caprio's lilacs to the USA national phenology network. *Front. Ecol. Environ.* **10**, 324–327 (2012).
48. Templ, B. et al. Pan European Phenological database (PEP725): a single point of access for European data. *Int. J. Biometeorol.* **62**, 1109–1113 (2018).
49. Ovaskainen, O. et al. Chronicles of nature calendar, a long-term and large-scale multitaxon database on phenology. *Sci. Data* **7**, 47 (2020).
50. Didan, K. MODIS/Terra Vegetation Indices 16-Day L3 Global 250m SIN Grid V061. NASA EOSDIS Land Processes DAAC <https://doi.org/10.5067/MODIS/MOD13Q1.061> (2021).
51. Gill, A. L. et al. Changes in autumn senescence in northern hemisphere deciduous trees: a meta-analysis of autumn phenology studies. *Ann. Bot.* **116**, 875–888 (2015).
52. Jeong, S.-J. et al. Phenology shifts at start vs. end of growing season in temperate vegetation over the Northern Hemisphere for the period 1982–2008. *Glob. Change Biol.* **17**, 2385–2399 (2011).
53. Menzel, A. et al. European phenological response to climate change matches the warming pattern. *Glob. Change Biol.* **12**, 1969–1976 (2006).
54. Piao, S. et al. Variations in satellite-derived phenology in China's temperate vegetation. *Glob. Change Biol.* **12**, 672–685 (2006).
55. Asshoff, R., Zotz, G. & Körner, C. Growth and phenology of mature temperate forest trees in elevated CO₂. *Glob. Change Biol.* **12**, 848–861 (2006).
56. Norby, R. J. et al. Net primary productivity of a CO₂-enriched deciduous forest and the implications for carbon storage. *Ecol. Appl.* **12**, 1261–1266 (2002).
57. Norby, R. J. et al. Fine-root production dominates response of a deciduous forest to atmospheric CO₂ enrichment. *Proc. Natl Acad. Sci. USA* **101**, 9689–9693 (2004).
58. Fang, K. et al. Influence of non-climatic factors on the relationships between tree growth and climate over the Chinese Loess Plateau. *Glob. Planet. Change* **132**, 54–63 (2015).
59. Xu, L. et al. Productivity and water use efficiency of *Pinus tabulaeformis* responses to climate change in the temperate monsoon region. *Agric. Meteorol.* **327**, 109188 (2022).
60. Niinemets, Ü. Components of leaf dry mass per area—thickness and density—alter leaf photosynthetic capacity in reverse directions in woody plants. *N. Phytol.* **144**, 35–47 (1999).
61. Thomas, S. C. & Winner, W. E. Photosynthetic differences between saplings and adult trees: an integration of field results by meta-analysis. *Tree Physiol.* **22**, 117–127 (2002).
62. Niinemets, Ü. & Sack, L. Structural determinants of leaf light-harvesting capacity and photosynthetic potentials. *Progress Bot.* **67**, 385–419 (2006).
63. Yoshimoto, M., Oue, H. & Kobayashi, K. Energy balance and water use efficiency of rice canopies under free-air CO₂ enrichment. *Agric. Meteorol.* **133**, 226–246 (2005).
64. Ainsworth, E. A. & Rogers, A. The response of photosynthesis and stomatal conductance to rising [CO₂]: mechanisms and environmental interactions. *Plant Cell Environ.* **30**, 258–270 (2007).
65. Zhang, S. et al. Tree species mixing can amplify microclimate offsets in young forest plantations. *J. Appl. Ecol.* **59**, 1428–1439 (2022).
66. Wang, S. et al. Recent global decline of CO₂ fertilization effects on vegetation photosynthesis. *Science* **370**, 1295–1300 (2020).
67. Friedl, M. & Sulla-Menashe, D. MODIS/Terra+Aqua Land Cover Type Yearly L3 Global 0.05Deg CMG V061. NASA EOSDIS Land Processes DAAC <https://doi.org/10.5067/MODIS/MCD12C1.061> (2022).
68. Potapov, P. et al. The global 2000–2020 land cover and land use change dataset derived from the Landsat archive: first results. *Front. Remote Sens.* **3**, 856903 (2022).
69. Su, Y. et al. Asymmetric influence of forest cover gain and loss on land surface temperature. *Nat. Clim. Change* **13**, 823–831 (2023).
70. Chuvieco, E., Pettinari, M. L., & Otón, G. ESA Fire Climate Change Initiative (Fire_cci): AVHRR-LTDR Burned Area Pixel product, version 1.1. Centre for Environmental Data Analysis <https://doi.org/10.5285/b1bd715112ca43ab948226d11d72b85e> (2020).
71. Abatzoglou, J. T. et al. TerraClimate, a high-resolution global dataset of monthly climate and climatic water balance from 1958–2015. *Sci. Data* **5**, 170191 (2018).
72. Wang, X. et al. A two-fold increase of carbon cycle sensitivity to tropical temperature variations. *Nature* **506**, 212–215 (2014).
73. Liu, L. et al. Tropical tall forests are more sensitive and vulnerable to drought than short forests. *Glob. Change Biol.* **28**, 1583–1595 (2022).
74. Besnard, S. et al. Mapping global forest age from forest inventories, biomass and climate data. *Earth Syst. Sci. Data Discuss.* **13**, 4881–4896 (2021).

75. Wang, S. et al. A TPE based inversion of PROSAIL for estimating canopy biophysical and biochemical variables of oilseed rape. *Comput. Electron. Agric.* **152**, 350–362 (2018).
76. Verhoef, W. Light scattering by leaf layers with application to canopy reflectance modeling: the SAIL model. *Remote Sens. Environ.* **16**, 125–141 (1984).
77. Verhoef, W. & Bach, H. Coupled soil–leaf–canopy and atmosphere radiative transfer modeling to simulate hyperspectral multi-angular surface reflectance and TOA radiance data. *Remote Sens. Environ.* **109**, 166–182 (2007).
78. Doughty, C. E. et al. Tropical forest leaves may darken in response to climate change. *Nat. Ecol. Evol.* **2**, 1918–1924 (2018).
79. Jacquemoud, S., & Ustin, S. *Leaf Optical Properties* (Cambridge Univ. Press, 2019).
80. Feret, J. et al. PROSPECT-4 and 5: advances in the leaf optical properties model separating photosynthetic pigments. *Remote Sens. Environ.* **112**, 3030–3043 (2008).
81. Jacquemoud, S. et al. PROSPECT Plus SAIL models: a review of use for vegetation characterization. *Remote Sens. Environ.* **113**, S56–S66 (2009).
82. Darvishzadeh, R. et al. Inversion of a radiative transfer model for estimating vegetation LAI and chlorophyll in a heterogeneous grassland. *Remote Sens. Environ.* **112**, 2592–2604 (2008).
83. Mousivand, A. et al. Global sensitivity analysis of the spectral radiance of a soil–vegetation system. *Remote Sens. Environ.* **145**, 131–144 (2014).
84. Breunig, F. M. et al. Spectral anisotropy of subtropical deciduous forest using MISR and MODIS data acquired under large seasonal variation in solar zenith angle. *Int. J. Appl. Earth Obs. Geoinf.* **35**, 294–304 (2015).
85. Yin, C. et al. Chlorophyll content estimation in arid grasslands from Landsat-8 OLI data. *Int. J. Remote Sens.* **37**, 615–632 (2016).
86. Rosseel, Y. lavaan: an R package for structural equation modeling. *J. Stat. Softw.* **48**, 1–36 (2012).
87. Wang, F. Code to support ‘Contrasting age-dependent leaf acclimation strategies driving vegetation greening across deciduous broadleaf forests in the middle to high latitudes’. *Zenodo* <https://doi.org/10.5281/zenodo.15765680> (2025).

Acknowledgements

This study was supported by the National Natural Science Foundation of China (grant nos. 42471326, 31971458 and U21A6001), the

National Key R&D Program of China (grant no. 2024YFF1306600) and the Science and Technology Program of Guangdong (grant no. 2024B1212070012).

Author contributions

X.C. designed the study, wrote the initial paper and revised the paper. F.W. and M.X. collected the data, performed the analysis, drew the figures and wrote the Methods section. L.Z., C.E.D., P.C., P.B.R., J.S., J.M.C., J.L., J.K.G., D.H., S.T., Y.J.S., Lingli Liu, J.X., H.W., K. Yu, Z.Z., P.Z., X.L., H.L., Y.Z., K. Yan, Liyang Liu, R.L., Y.S., Y.M., Y.P., X.Y., Y.H.F., N.H. and W.Y. contributed to discussing the scientific question, as well as writing and revising the paper.

Competing interests

The authors declare no competing interests.

Additional information

Supplementary information The online version contains supplementary material available at <https://doi.org/10.1038/s41477-025-02096-5>.

Correspondence and requests for materials should be addressed to Xiuzhi Chen.

Peer review information *Nature Plants* thanks Rakesh Tiwari and the other, anonymous, reviewer(s) for their contribution to the peer review of this work.

Reprints and permissions information is available at www.nature.com/reprints.

Publisher's note Springer Nature remains neutral with regard to jurisdictional claims in published maps and institutional affiliations.

Springer Nature or its licensor (e.g. a society or other partner) holds exclusive rights to this article under a publishing agreement with the author(s) or other rightsholder(s); author self-archiving of the accepted manuscript version of this article is solely governed by the terms of such publishing agreement and applicable law.

© The Author(s), under exclusive licence to Springer Nature Limited 2025

Fangyi Wang^{1,25}, **Meimei Xue**^{1,25}, **Liming Zhou**², **wChristopher E. Doughty**³, **Philippe Ciais**⁴, **Peter B. Reich**^{5,6}, **Jiali Shang**⁷, **Jing Ming Chen**⁸, **Jane Liu**⁸, **Julia K. Green**³, **Dalei Hao**⁹, **Shengli Tao**¹⁰, **Yanjun Su**¹¹, **Lingli Liu**¹¹, **Jianyang Xia**¹², **Han Wang**¹³, **Kailiang Yu**¹⁴, **Zaichun Zhu**¹⁵, **Peng Zhu**¹⁶, **Xing Li**¹, **Hui Liu**¹⁷, **Yelu Zeng**¹⁸, **Kai Yan**¹⁹, **Liyang Liu**⁴, **Raffaele Laforcezza**²⁰, **Yongxian Su**²¹, **Yanqiong Meng**²², **Yixuan Pan**¹, **Xueqin Yang**¹, **Yongshuo H. Fu**¹⁹, **Nianpeng He**²³, **Wenping Yuan**²⁴ & **Xiuzhi Chen**¹✉

¹Guangdong Province Data Center of Terrestrial and Marine Ecosystems Carbon Cycle, School of Atmospheric Sciences, School of Ecology, Sun Yat-sen University, Zhuhai, China. ²Department of Atmospheric and Environmental Sciences, University at Albany, State University of New York, Albany, NY, USA. ³School of Informatics, Computing, and Cyber Systems, Northern Arizona University, Flagstaff, AZ, USA. ⁴Laboratoire des Sciences du Climat et de l'Environnement, IPSL, CEA-CNRS-UVSQ, Université Paris-Saclay, Gif sur Yvette, France. ⁵Institute for Global Change Biology and School for Environment and Sustainability, University of Michigan, Ann Arbor, MI, USA. ⁶Department of Forest Resources, University of Minnesota, St. Paul, MN, USA. ⁷Ottawa Research and Development Centre, Agriculture and Agri-Food Canada, Ottawa, Ontario, Canada. ⁸Department of Geography and Planning, University of Toronto, Toronto, Ontario, Canada. ⁹Atmospheric Sciences and Global Change Division, Pacific Northwest National Laboratory, Richland, WA, USA. ¹⁰Institute of Ecology, Peking University, Beijing, China. ¹¹State Key Laboratory of Vegetation and Environmental Change, Institute of Botany, Chinese Academy of Sciences, Beijing, China. ¹²School of Ecological and Environmental Sciences, East China Normal University, Shanghai, China. ¹³Department of Earth System Science, Ministry of Education Key Laboratory for Earth System Modeling, Institute for Global Change Studies, Tsinghua University, Beijing, China. ¹⁴Institute of Geographical Sciences and Natural Resources Research, Chinese Academy of Sciences, Beijing, China. ¹⁵School of Urban Planning and Design, Peking University, Beijing, China. ¹⁶School of Biological Sciences, The University of Hong Kong, Hong Kong, China. ¹⁷South China Botanical Garden, Chinese Academy of Sciences, Guangzhou, China. ¹⁸College of Land Science and Technology, China Agricultural University, Beijing, China.

¹⁹Center for GeoData and Analysis, State Key Laboratory of Remote Sensing Science, Faculty of Geographical Science, Beijing Normal University, Beijing, China. ²⁰Department of Agricultural and Environmental Sciences, University of Bari 'A. Moro', Bari, Italy. ²¹State Key Laboratory of Urban and Regional Ecology, Research Center for Eco-Environmental Sciences, Chinese Academy of Sciences, Beijing, China. ²²School of Forestry and Landscape Architecture, Anhui Agricultural University, Hefei, China. ²³School of Forestry, Northeast Forestry University, Harbin, China. ²⁴College of Urban and Environmental Sciences, School of Urban Planning and Design, Peking University, Beijing, China. ²⁵These authors contributed equally: Fangyi Wang, Meimei Xue. ✉ e-mail: chenxzh73@mail.sysu.edu.cn